

# Energy & Environmental Science

Accepted Manuscript



This is an *Accepted Manuscript*, which has been through the Royal Society of Chemistry peer review process and has been accepted for publication.

*Accepted Manuscripts* are published online shortly after acceptance, before technical editing, formatting and proof reading. Using this free service, authors can make their results available to the community, in citable form, before we publish the edited article. We will replace this *Accepted Manuscript* with the edited and formatted *Advance Article* as soon as it is available.

You can find more information about *Accepted Manuscripts* in the [Information for Authors](#).

Please note that technical editing may introduce minor changes to the text and/or graphics, which may alter content. The journal's standard [Terms & Conditions](#) and the [Ethical guidelines](#) still apply. In no event shall the Royal Society of Chemistry be held responsible for any errors or omissions in this *Accepted Manuscript* or any consequences arising from the use of any information it contains.

## PAPER

[View Article Online](#)  
[View Journal](#)

Cite this: DOI: 10.1039/xxxxxxxxxx

## Intrinsic femtosecond charge generation dynamics in single crystal $\text{CH}_3\text{NH}_3\text{PbI}_3$

 David A. Valverde-Chávez,<sup>a</sup> Carlito Ponseca Jr.,<sup>b</sup> Constantinos Stoumpos,<sup>c</sup> Arkady Yartsev,<sup>b</sup> Mercuri G. Kanatzidis,<sup>c</sup> Villy Sundström,<sup>b</sup> and David G. Cooke<sup>a\*</sup>

 Received Date  
 Accepted Date

DOI: 10.1039/xxxxxxxxxx

www.rsc.org/journalname

Hybrid metal-organic perovskite solar cells have astounded the solar cell community with their rapid rise in efficiency while maintaining low-cost fabrication. The intrinsic material photophysics related to the generation of free charges, their dynamics and efficiency, however, remains to be understood. As fabrication techniques improve, larger crystal grain sizes have been shown to be a critical factor for improving both the optical and transport properties of the hybrid metal halide perovskites. In this work, we use pulses of multi-THz frequency light in the ultra-broadband 1 - 30 THz (4 - 125 meV) range to observe the ac conductivity in large single crystal  $\text{CH}_3\text{NH}_3\text{PbI}_3$ . Our spectra reveal the ultrafast dynamics and efficiencies of free charge creation and extremely high charge carrier mobility as high as 500 - 800  $\text{cm}^2/\text{Vs}$ . While quasi-equilibrium analysis of efficiencies through the Saha equation suggests a binding energy on the order of 49 meV, an observed reflectance feature appearing at high pump fluence occurs at 12 meV and is consistent with an orbital transition of the exciton, indicating a much lower Rydberg energy of 17 meV at room temperature. The signature of the exciton is found to vanish on a 1 ps time scale commensurate with the appearance of mobile carriers, consistent with thermal dissociation of the exciton to the continuum in the room temperature tetragonal phase.

### Introduction

The impressive photovoltaic,<sup>1</sup> water photolysis,<sup>2</sup> and even lasing<sup>3</sup> properties of hybrid metal halide perovskites, combined with a composition of earth abundant elements, low fabrication cost and rapid energy payback time,<sup>4</sup> shows great promise for next generation solution processable optoelectronic devices. The overall power conversion efficiency of organo-metal halide perovskite solar cells has climbed to 20.1% in a span of only three years<sup>5,6</sup>, the fastest rate of increase compared to all other solar cell technologies. This fast pace in device development has been matched by a flurry of spectroscopic investigations attempting to understand the intrinsic charge generation, recombination and transport properties of these materials.<sup>7-24</sup> A key spectral region for these materials is 1 - 100 meV, encompassing the proposed exciton binding energy that determines the charge photogeneration efficiency<sup>15,25</sup>, carrier scattering rates governing charge transport, and lattice vibrations whose role in screening the exciton remains controversial.<sup>16,26</sup> Time-resolved terahertz spectroscopy

(TRTS) is a powerful technique to probe these low energy excitations immediately after photoexcitation on femtosecond time scales.<sup>27</sup> Previous THz studies on the trihalide and mixed halide perovskites have focused on frequency-averaged THz absorption, probing energies below 10 meV.<sup>9,11,25</sup> These measurements on thin film samples have placed initial lower limits on the mobility, shown suppressed bi-molecular recombination, and indicated the role of the exciton binding energy in the generation of free charges on a  $\sim 2$  ps time scale.<sup>9</sup> A very recent TRTS study performing full energy resolved spectroscopy on  $\text{CH}_3\text{NH}_3\text{PbI}_3$  thin films over a relatively low 2 THz bandwidth observed a conductivity spectrum dominated by the disorder of the polycrystalline films and focused on the long time recombination dynamics occurring over several hundreds of picoseconds.<sup>24</sup>

In this work, we concern ourselves with the intrinsic sub-picosecond dissociation dynamics of excitons and generation of charges in single crystal  $\text{CH}_3\text{NH}_3\text{PbI}_3$ . Only recently have large single crystals of the hybrid metal halide perovskites become available, showing impressive charge transport characteristics including mobilities as high as 150  $\text{cm}^2/\text{Vs}$  and diffusion lengths over 100  $\mu\text{m}$ .<sup>28-32</sup> We perform complete energy and time-resolved ultra-broadband THz spectroscopy in the 4-125 meV spectral range (30 THz bandwidth) on a large single crystal of the hybrid metal halide perovskite  $\text{CH}_3\text{NH}_3\text{PbI}_3$ . Femtosecond

<sup>a</sup> Department of Physics, McGill University, Montreal, QC, Canada H3A 2T8. Fax: +1 514 398 8434; Tel: +1 514 398 6490; E-mail: cooke@physics.mcgill.ca

<sup>b</sup> Division of Chemical Physics, Lund University, Box 124, 221 00 Lund, Sweden.

<sup>c</sup> Department of Chemistry, Northwestern University, Evanston, Illinois 60208, United States.

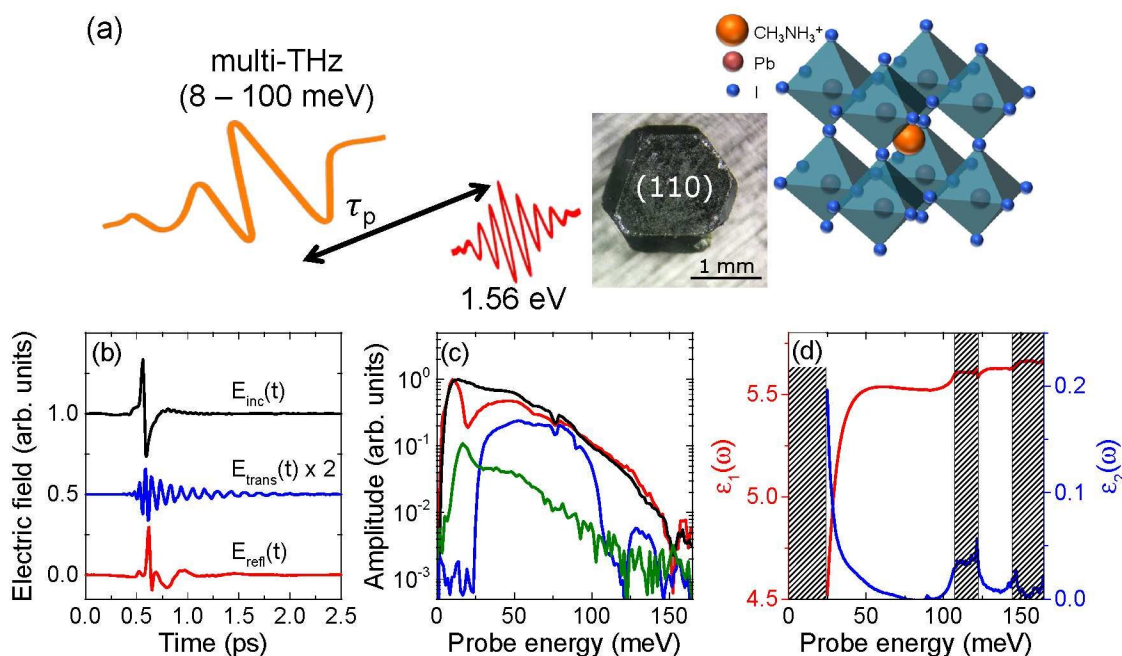


**Fig. 1** (a) A schematic of the time-resolved multi-THz spectroscopy experiment is given, where a 40 fs, 1.56 eV pump pulse photoexcites the  $\text{CH}_3\text{NH}_3\text{PbI}_3$  crystal at normal incidence, colinearly with a multi-THz probe pulse with Fourier spectral components spanning 1 - 30 THz (4 - 125 meV). The sample is a single crystal  $\text{CH}_3\text{NH}_3\text{PbI}_3$  approximately 1.5 x 1.5 mm in size with the (110) facet (indexed in the cubic setting) as the probed surface. (b) In the absence of a photoexcitation, the incident (black), transmitted (blue) and reflected (red) multi-THz pulses after interaction with the crystal are shown with (c) corresponding Fourier amplitude spectra. The amplitude of the pump-induced differential reflected field,  $|\Delta E(\omega, 600\text{fs})|$ , is also shown in green. (d) The dark state dielectric function probing the (110) plane in transmission, with areas of no information indicated by the hatched regions.

photoexcitation at the band edge probes the kinetics of mobile charge generation via dissociation of excitons, without the influence of excess kinetic energy, with 40 fs temporal resolution. Our greatly enhanced bandwidth reveals the conductivity spectrum in the THz band is dominated completely by mobile charge screening of a large optically-active phonon, not considered in previous TRTS work. Accounting for the dispersion of the phonon, a simple Drude conductivity spectrum is revealed, permitting direct extraction of charge densities and mobilities in the absence of disorder. We observe remarkably high carrier mobilities for single crystals that reach  $800\text{ cm}^2/\text{Vs}$  on ultra-short time scales and analyze our results under the assumption of quasi-equilibrium to yield an exciton binding energy of  $49 \pm 3\text{ meV}$ . A more direct measurement of the exciton is found at high photoexcitation densities, where an orbital transition indicates a much lower binding energy of approximately 17 meV for the room temperature tetragonal phase.<sup>28</sup> We discuss this apparent discrepancy and point towards future work required to understand the nature of the exciton in this material.

## Methods

### Sample preparation

Single-crystals of  $\text{CH}_3\text{NH}_3\text{PbI}_3$  suitable for characterization were grown from a solvent mixture comprising of aqueous HI (57% w/w, 5.1 mL) and aqueous  $\text{H}_3\text{PO}_2$  (50% w/w, 1.7 mL). In a typical procedure, a 20 mL scintillation vial was charged with the colorless solvent mixture and heated to boiling (ca. 120° C).

Addition of solid PbO (670 mg, 3 mmol) and  $\text{CH}_3\text{NH}_3\text{Cl}$  (202 mg, 3 mmol) led initially to the formation of a black precipitate which rapidly dissolved leading to a clear bright yellow solution. The boiling hot solution was then capped with several layers of parafilm tape to ensure that the composition of the vapors was maintained throughout the crystal growth process. Omission of this step leads to the crystallization of  $\text{CH}_3\text{NH}_3\text{PbI}_3 \cdot \text{H}_2\text{O}$ , instead. On standing, upon reaching ambient temperature a countable number (in the range of 10-100) of small  $\text{CH}_3\text{NH}_3\text{PbI}_3$  crystals begin to form, which act as initial seeds for the subsequent crystal growth from the supersaturated supernatant solution. Well-formed, faceted crystals of rhombic dodecahedral crystal habit were obtained after 2 weeks with crystal sizes ranging from 1-4 mm among several batches, with the size of the crystals being inversely proportional to the number of the initial crystal seeds. The crystals were collected manually by decanting the mother liquor, pressed dry with a soft filtration paper and thoroughly dried under a stream of  $\text{N}_2$  gas.

### THz spectroscopy

Fig 1(a) shows the schematic of the optical pump – multi-THz probe measurement of the large,  $\text{mm}^3$  sized single crystal of  $\text{CH}_3\text{NH}_3\text{PbI}_3$ , probing the (110) facet (in the cubic setting or (100) in the tetragonal setting)<sup>28</sup> of the crystal with image provided. The unit cell of the cubic phase is also shown, with the average position of the  $\text{CH}_3\text{NH}_3^+$  cation indicated by the orange ball in the center of the unit cell. In these experiments, an op-

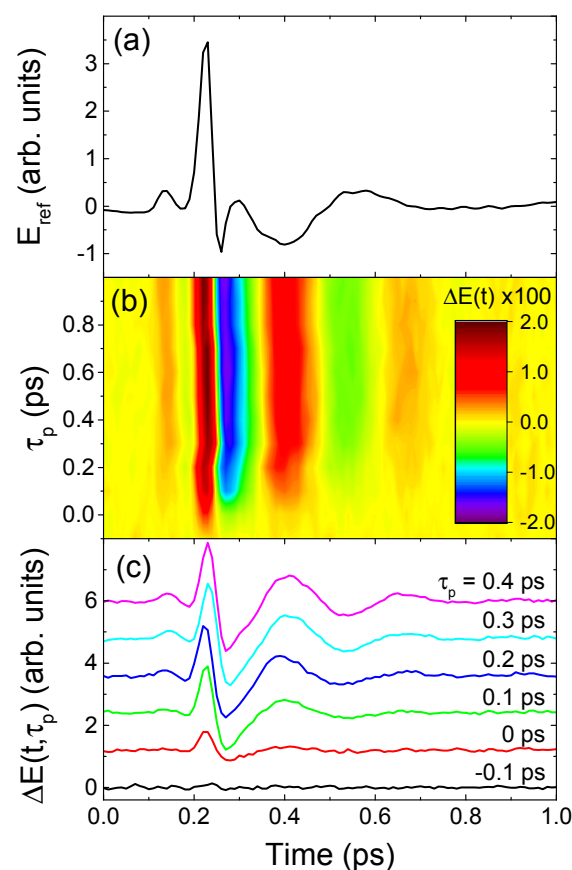


**Fig. 2** (a) The reflected THz transient from the unexcited  $\text{CH}_3\text{NH}_3\text{PbI}_3$  crystal (110) facet and (b) the two-dimensional  $\Delta E(t, \tau_p) = E_{\text{pump}}(t, \tau_p) - E_{\text{ref}}(t)$  data set for pump-probe delay times  $\tau_p < 1$  ps. (c) Selected cuts in the map along constant  $\tau_p$  are shown, representing the buildup of photoconductivity in the crystal.

tical pulse photoexcites the sample and the induced charge degrees of freedom are then probed by transmission or reflection of a phase-stable, single cycle electromagnetic transient with frequency components in the THz range, called a THz pulse. Charge carriers and excitons are excited in the sample by the pump beam resonant with the band edge at 1.56 eV to minimize initial excess energy, thereby suppressing direct exciton dissociation through this channel.<sup>33</sup> The penetration depth of the pump pulse is taken to be 1  $\mu\text{m}$  determined by thin film absorption,<sup>34</sup> and it is assumed this is the same for a single crystal. Multi-THz pulses are generated via a two-colour laser plasma in dry air and the electric field is directly detected after normal incidence reflection off the crystal facet by an air-biased coherent detection scheme with 30 THz bandwidth.<sup>27</sup> All measurements were performed under dry air environment and no evidence of oxidation was observed during the experiments.

## Results

The incident THz pulse ( $E_{\text{inc}}$ ), is shown in Fig. 1(b) along with the transmitted ( $E_{\text{trans}}$ ) and reflected ( $E_{\text{refl}}$ ) pulses in the absence of a photoexcitation. The ultra-broadband THz pulse  $E_{\text{inc}}(t)$  contains spectral components from 1 - 30 THz (4-125 meV or 33-

1000  $\text{cm}^{-1}$ ), as shown in the corresponding Fourier amplitude spectrum in Fig 1(c). While the reflected pulse retains all incident Fourier components with noticeable dispersion,  $E_{\text{trans}}(t)$  is strongly chirped with no spectral components below 25 meV due to absorption and reflection arising from an infrared active phonon and dielectric relaxation of the  $\text{CH}_3\text{NH}_3^+$  cation.<sup>35</sup> The change of amplitude and phase of the THz pulse after transmission provides the complex dielectric function  $\tilde{\epsilon}(\omega) = \epsilon_1(\omega) + i\epsilon_2(\omega)$  via inversion of the Fresnel equations, and is shown in Fig. 1(d). The spectra is dominated by an infrared-active Pb-I bond stretching mode at  $\sim 8$  meV, previously observed in Raman and THz spectroscopy<sup>10,36</sup> which happens to overlap with a breathing of the  $\text{PbI}_6$  octahedra coupled with librational motion of the  $\text{CH}_3\text{NH}_3^+$  cation, as calculated recently in Ref. 37. Higher frequency vibrational modes are observed at 112 meV and 155 meV, in agreement with Ref. 38 and associated with the C-N bond vibrations. In addition, a broad GHz dielectric contribution has also been identified from microwave measurements due to the relaxation of the  $\text{CH}_3\text{NH}_3^+$  cation.<sup>26</sup> The  $\text{CH}_3\text{NH}_3^+$  group is free to rotate and undergo librations in the room temperature tetragonal phase giving a Debye contribution to the dielectric function with a picosecond relaxation time. As a result of these two lattice responses, the optical transmission is strongly suppressed for energies below 25 meV. The real dielectric function,  $\epsilon_1(\omega)$ , responsible for renormalizing the Coulomb interaction of injected electrons and holes and therefore the exciton binding energy  $E_B$ ,<sup>13,34</sup> is nearly constant at 5.5 for 40 - 100 meV range. Below 40 meV near resonant with the exciton binding energy, however,  $\epsilon_1(\omega)$  is quite dispersive. The dynamics of exciton-phonon coupling should therefore be considered when discussing the appropriate dielectric function.<sup>35</sup>

We now turn to the time-resolved THz spectra after photoexcitation. The reference multi-THz waveform in the absence of optical pumping,  $E_{\text{ref}}(t)$ , is shown in Fig. 1(b) and Fig. 2(a) after normal incidence reflection from the (110) crystal facet, showing slight reshaping due to the dispersion of the crystal. The pump-induced change in the reflected THz electric field  $\Delta E(t, \tau_p) = E_{\text{pump}}(t, \tau_p) - E_{\text{ref}}(t)$  at a given pump-probe delay time  $\tau_p$  is measured at variable delays producing the two-dimensional time-domain data set shown in Fig. 2(b). Both  $E_{\text{ref}}(t)$  and  $\Delta E(t, \tau_p)$  are measured simultaneously through a double modulation scheme, required to eliminate the influence of systematic timing variations.<sup>39</sup> The Fourier amplitude of the modulated field in quasi-equilibrium is given in Fig. 1(c), showing spectral information is obtained between 8 - 80 meV. The significant phase shift compared to the reference pulse indicates a strong change in the dispersion after charges are photo-injected into the crystal. This is a signature of injected mobile charges screening the lattice from the applied field, within the pump pulse penetration depth of 1  $\mu\text{m}$  in the crystal.<sup>34</sup> The amplitude of the  $\Delta E(t, \tau_p)$  response, proportional to the pump-induced photoconductivity in the sample, reaches its maximum within 400 fs after photoexcitation as seen in the differential waveforms in Fig. 2(c) for variable  $\tau_p$ . We note that this is 10 times the temporal resolution of our technique and thus mobile carriers are not generated instantaneously but rather through exciton dissociation.<sup>25</sup>

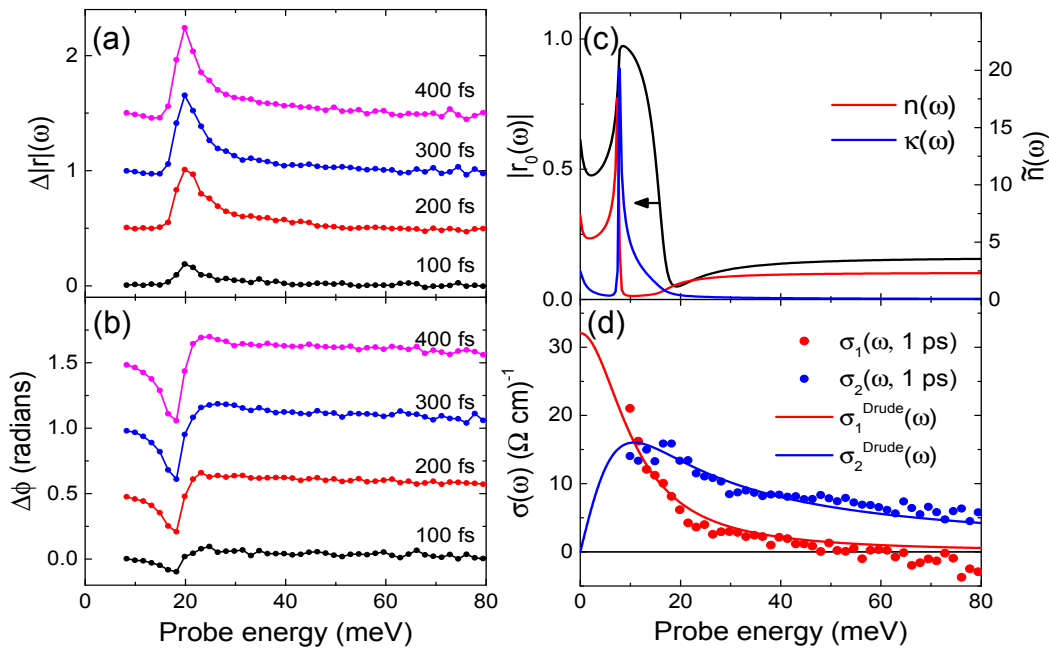


**Fig. 3** (a) Amplitude and (b) phase of the differential multi-THz reflectance shifted by steps of 0.5 for clarity. (c) The model of the complex index of refraction of the unexcited crystal used to describe the substrate dispersion and extract the complex photoconductivity. (d) The complex conductivity spectrum with Drude spectrum fits recorded at 1 ps following excitation.

The corresponding spectral amplitude and phase of the pump-induced change in THz reflectance, defined as  $\Delta\tilde{r}(\omega, \tau_p) = \Delta\tilde{E}(\omega, \tau_p)/\tilde{E}_{ref}(\omega)$ , are shown in Fig. 3(a) and (b), respectively for pump-probe times from 0 - 400 fs at a pump fluence of  $80 \mu\text{J}/\text{cm}^2$ . The data can be understood by the analytic formula:<sup>27</sup>

$$\Delta\tilde{r}(\omega, \tau_p) = -\left(\frac{1 + \tilde{r}_0}{\tilde{r}_0}\right) \frac{Z_0 d \tilde{\sigma}(\omega, \tau_p)}{1 + \tilde{n}(\omega) + Z_0 d \tilde{\sigma}(\omega, \tau_p)} \quad (1)$$

where  $\tilde{\sigma} = \sigma_1 + i\sigma_2$  is the complex ac photoconductivity,  $\tilde{n} = n + i\kappa$  is the complex crystal index of refraction and  $\tilde{r}_0$  is the complex crystal reflection coefficient given by  $\tilde{r}_0 = (1 - \tilde{n})/(1 + \tilde{n})$ . In the absence of photoconductivity,  $\Delta\tilde{r}(\omega) = 0$  as well as in the limit for a highly reflective crystal with  $n \gg 1$  where  $r_0 \rightarrow -1$ . Fig. 3(c) shows the complex index of refraction of the crystal used to describe  $\tilde{r}_0$ , composed of a picosecond Debye dielectric relaxation and Lorentzian response modelling the 8 meV infrared active phonon in agreement with Fig. 1(d). The background complex refractive index of the crystal  $\tilde{n}(\omega) = \sqrt{\tilde{\epsilon}(\omega)}$  and the dielectric function  $\tilde{\epsilon}(\omega)$  is given by the Lorentzian phonon and Debye components

$$\tilde{\epsilon}(\omega) = \epsilon_\infty + \frac{\omega_p^2}{\omega_0^2 - \omega^2 - i\omega\gamma} + \frac{\epsilon_s}{1 - i\omega\tau_D} \quad (2)$$

The high frequency dielectric function  $\epsilon_\infty = 5.5$  determined from transmission measurements in Fig. 1(d), the Pb-I bending mode  $\omega_0/2\pi = 1.96$  THz and the Debye relaxation time  $\tau_D = 2.5$  ps with a low energy limit from literature  $\epsilon_s \approx 30$ .<sup>26</sup> The spectra were found to be relatively insensitive to the phonon relaxation rate, set to a reasonable  $\gamma = 0.1$  THz. The corresponding reflectivity amplitude  $|r_0|$  is shown in Fig. 3(c) exhibiting a sharp drop to

a minimum just below 20 meV. Thus the screening of the lattice by injected mobile charge carriers is responsible for the large  $\Delta r$  response observed in Fig. 3(a), and by Kramers-Kronig the corresponding phase change in Fig. 3(b). By inversion of Eq. 1, the complete  $\tilde{\sigma}(\omega, \tau_p)$  spectra can be extracted in temporal slices following photoexcitation, revealing the underlying ultrafast charge transport characteristics.

An example of the  $\tilde{\sigma}(\omega, \tau_p)$  spectrum recorded at  $\tau_p = 1$  ps after excitation is shown in Fig. 3(d). The data is very well described by a simple Drude model  $\tilde{\sigma}(\omega) = \frac{n_D e^2 \tau}{m^*} \frac{1}{1 - i\omega\tau}$ , where  $n_D$  is the mobile charge density and  $\tau$  is the momentum scattering time determining the charge carrier mobility through the relation  $\mu = e\tau/m^*$  with  $m^* = 0.2m_e$  being the charge carrier effective mass<sup>40</sup>. The Drude response confirms the band nature of transport in the single crystal  $\text{CH}_3\text{NH}_3\text{PbI}_3$  as opposed to charges in a disordered film where hopping conductivity occurs. The scattering time  $\tau$  can be estimated simply by the crossing point of  $\sigma_1$  and  $\sigma_2$ , occurring at an energy  $h/(2\pi\tau) \approx 10$  meV. This provides an estimate of  $\tau \sim 70$  fs corresponding to a remarkably high  $\mu \sim 620$   $\text{cm}^2/\text{Vs}$  for a solution processed semiconductor. This measurement represents the highest mobility observed in these materials to date although recent improvements in grain size and large crystal fabrication have seen  $\mu$  on the order of  $150$   $\text{cm}^2/\text{Vs}$ .<sup>29,30</sup> Moreover, the amplitude of the photoconductivity directly yields the mobile carrier density  $n_D \approx 3.3 \times 10^{17} \text{ cm}^{-3}$ , estimated by the Drude dc limit  $\sigma_{dc} = n_D e \mu$ . The mobile charge carrier generation efficiency is given by  $x = n_D/n_{ph} \approx 12\%$  where  $n_{ph} = 2.9 \times 10^{18} \text{ cm}^{-3}$  is the absorbed photon density given the pump fluence of  $80 \mu\text{J}/\text{cm}^2$  and the 10% reflection of the pump at  $795 \text{ nm}$ .<sup>41</sup> This result is consistent with the expected result of the Saha-Langmuir equa-

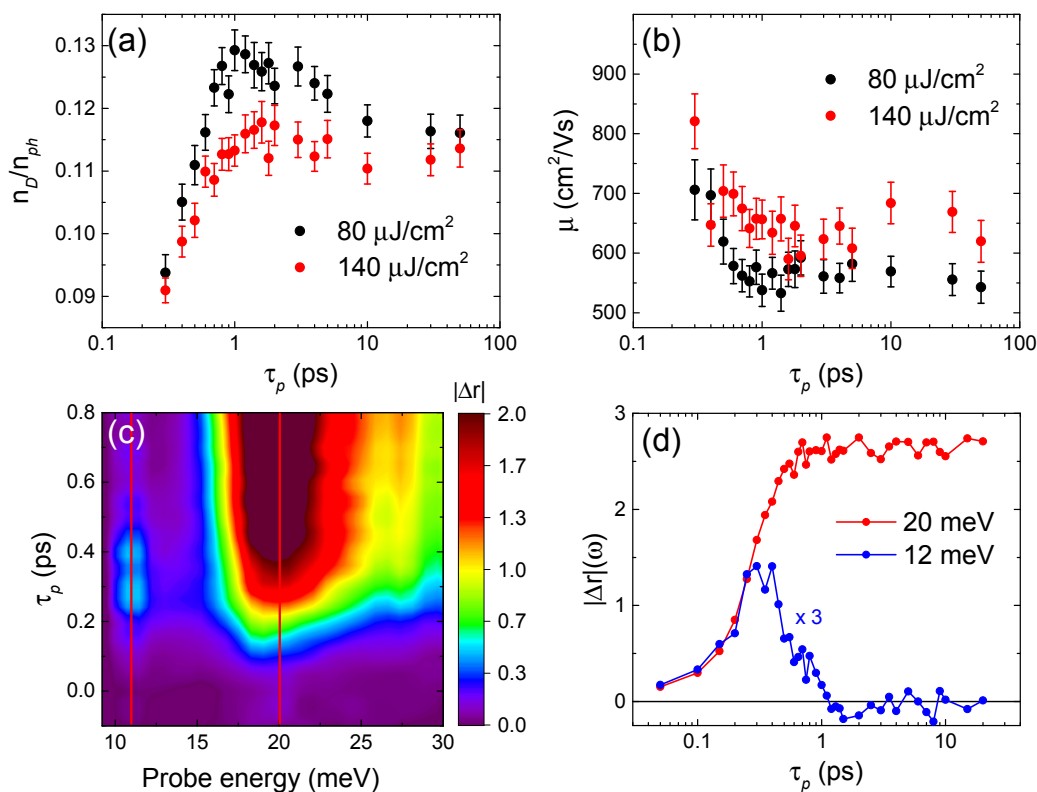


**Fig. 4** (a) The mobile charge carrier generation efficiency defined as the ratio of the charge density to the absorbed photon density, at pump fluences of 80 and 140  $\mu\text{J}/\text{cm}^2$ . (b) Charge carrier mobility derived from the 80 and 140  $\mu\text{J}/\text{cm}^2$  data sets with global complex fits to the Drude model. (c) The two-dimensional data set of the differential reflectance amplitude at a fluence of 810  $\mu\text{J}/\text{cm}^2$ , showing the early time region where a low energy transient peak appears at  $\approx 12$  meV. Vertical lines indicate cut regions shown in (d) at 12 meV and 20 meV corresponding to exciton and free charges, respectively. The dynamics of exciton dissociation are represented by the decay of the 12 meV peak concomitant with the 1 ps free charge density risetime.

tion defined as:<sup>15</sup>

$$\frac{x^2}{1-x} = \frac{1}{n_{\text{phot}}} \left( \frac{2\pi m_{\text{ex}} k_B T}{h^2} \right)^{3/2} e^{-\frac{E_B}{k_B T}} \quad (3)$$

assuming an exciton binding energy  $E_B = 50$  meV at 293 K using an exciton effective mass  $m_{\text{ex}} = 0.11 m_e$ .<sup>40</sup>

The results of global fitting of the Drude model to the complete two-dimensional time-frequency  $\tilde{\sigma}(\omega)$  maps, fitting both real and imaginary components simultaneously, are shown in Fig. 4. The dynamics of the mobile charge generation efficiency for two pump fluences is shown in Fig. 4(a), exhibiting a slight transient enhancement for  $\tau_p < 10$  ps at the lower fluence. The Saha-Langmuir equation accounts for this behaviour predicting a decrease in efficiency to 10% for the elevated fluence due to the greater probability of electron-hole binding.<sup>15</sup> The remaining  $\sim 90\%$  of excitations, however are bound excitons that are unable to screen the lattice directly due to their charge neutrality. If pump photons excite carriers above the band edge, however, exciton dissociation will be influenced by the initial excess kinetic energy, providing higher mobile charge yields. The goal of this study, however, is to probe the energetics of thermal dissociation governed solely by the exciton binding energy and so we leave this to future work. The mobility is also extracted through the Drude fits as  $\mu = e\tau/m^*$  and is found to be relatively fluence inde-

pendent, as shown in Fig. 4(b). A  $\approx 20\%$  decrease is observed in carrier mobility on a sub-picosecond time scale, which we conjecture could be due to the charging of trap states or some charge-mediated phonon scattering mechanism. Despite the slight reduction in the transient mobility, the steady-state mobility of 550  $\text{cm}^2/\text{Vs}$  is orders of magnitude higher than other solution processed semiconductors. Such a high intrinsic charge carrier mobility points towards future improvements in photovoltaic power conversion efficiencies.

The induced mobile charges, however, should also screen the exciton as discussed in a recent observation of band filling effects,<sup>14</sup> and so one expects more efficient generation at very high carrier densities. The critical Mott density that defines the threshold for the efficiency of this screening, however, has been estimated at  $n_{\text{crit}} \approx 1 \times 10^{18} \text{ cm}^{-3}$ , nearly an order of magnitude higher than densities in Fig. 3. To investigate the effects of charge screening of the exciton, a two-dimensional data set was taken at  $F = 810 \mu\text{J}/\text{cm}^2$  with the  $|\Delta r(\omega)|$  map shown in Fig. 4(c). The response is not well described by a Drude model alone, as it exhibits a transient low energy peak at 12 meV, below the main reflection peak at 20 meV. The dynamics of this excitation are shown by the vertical cuts in the map along the  $\tau_p$  axis for the two peaks and plotted in Fig. 4(d). The onset of the lattice screening occurs on a time scale of 0.5 - 1 ps, larger than the 40 fs temporal resolution of

the measurement and indicating the charge generation is driven by exciton dissociation. The 12 meV exciton peak initially tracks the rise time of the free charge 20 meV peak, however decays to the noise level by the time the lattice response is fully screened at  $\tau_p = 1$  ps. This indicates a coupling between the two excitations and we conclude that the 12 meV peak is due to an intra-excitonic orbital transition given the binding energies for trap states have been recently estimated to be much larger, on the order of 100 - 400 meV from the band edge.<sup>42</sup> We note if excitation into trap states was the dominant photoexcitation at the band edge, one would not expect a Drude conductivity spectrum but rather a conductivity which is activated at a characteristic frequency. Even if the quantum efficiency reaches 4.5% predicted by the Saha-Langmuir equation at this elevated fluence,  $n_D \approx 1.3 \times 10^{18} \text{ cm}^{-3}$  which exceeds  $n_{crit}$ . In this regime, one expects all excitons are dissociated forming an uncorrelated plasma. The disappearance of the 12 meV peak could be due to the dynamic screening of the injected exciton population as the density increases beyond the critical Mott density on a sub-picosecond time scale. In this case we would also expect a frequency shift of the peak to lower energies as the charge density increases, which we do not see. We note that previous THz work investigating the Mott criterion for silicon has not observed this softening either.<sup>43</sup> The non-instantaneous rise time of the excitonic peak can be explained by considering the bandwidth of the pump pulse resulting in a non-resonant excitation to the ground state and it taking time for the many-body Coulomb correlations to build, forming an exciton.<sup>33</sup>

The 12 meV peak is likely connected with the transition with the largest dipole moment, or an 1s - 2p transition which is typically 70% of the exciton Rydberg energy. This would suggest an exciton binding energy of approximately 17 meV in the room temperature tetragonal phase, in agreement with recent magneto-absorption measurements for the low temperature orthorhombic phase.<sup>22</sup> This is inconsistent however with their expectation of a critical collapse of the binding energy at room temperature to values on the order of 5 meV. A more detailed understanding of the broadband dielectric function in the THz range at low temperatures is required and will be the topic of future work. Finally, we note that our quasi-equilibrium analysis has yielded a value consistent with several previous works employing the Saha equation, yet is in disagreement with the more direct measurement of an orbital transition of the exciton. Miyata et al. in Ref. 22 partially explained this discrepancy between their findings and those of others who find  $E_B \sim 50$  meV by assuming their films were much more crystalline. Our single crystal measurements, however, show this result is present even in the absence of disorder. One possible cause could be a more complicated internal energetic structure of the exciton given the near resonance with a strong lattice vibration.<sup>35</sup> A better understanding of these materials will clearly require a detailed mapping of the dielectric function over relevant excitonic energy scales and temperature spanning structural transitions.

## Conclusions

In conclusion, we have performed optical pump - multi-THz spectroscopy on a single crystal lead halide perovskite in the 8 - 100

meV spectral region relevant to the exciton. Our spectra reveal the dynamic screening of infrared active phonons and the background Debye relaxation of the  $\text{CH}_3\text{NH}_3^+$  cation by the photo-generated free charge population. The sub-picosecond conductivity spectra directly reveals free charge densities and remarkably high mobilities of  $\sim 800 \text{ cm}^2/\text{Vs}$  on sub-picosecond time scales. Charge generation proceeds via exciton dissociation which is complete after 1 ps, much longer than the 40 fs temporal resolution of the technique. Analysis of the quantum yield of free charges using a quasi-equilibrium Saha equation predicts an exciton binding energy of  $49 \pm 3$  meV, however a more direct signature of an orbital excitonic transition at 12 meV is observed that indicates a binding energy on the order of 17 meV. The disagreement between the two may lie in the assumption of quasi-equilibrium or in a more detailed energetic structure of the exciton due to interaction with a near resonant phonon. The signature of the exciton is observed at densities above the Mott criterion where the Coulomb interaction is dynamically screened and they dissociate into free carriers.

## Acknowledgements

DC acknowledges funding from CFI, NSERC, and FQRNT and DV acknowledges a scholarship from the National Council of Science and Technology in Mexico (CONACYT). The Swedish Energy Agency (STEM), the Swedish Research Council, the Knut & Alice Wallenberg foundation and the European Research Council (Advanced Investigator Grant to VS, 226136-VISCHEM) are acknowledged. The nanometer Consortium at Lund University (nmc@LU) is also acknowledged. At Northwestern University the work was supported by the grant SC0012541 funded by the U.S. Department of Energy Office of Science.

## References

- 1 M. Liu, M. B. Johnston and H. J. Snaith, *Nature*, 2013, **501**, 395–398.
- 2 J. Luo, J.-H. Im, M. T. Mayer, M. Schreier, M. K. Nazeeruddin, N.-G. Park, S. D. Tilley, H. J. Fan and M. Grätzel, *Science*, 2014, **345**, 1593–1596.
- 3 F. Deschler, M. Price, S. Pathak, L. E. Klintberg, D.-D. Jarausch, R. Högler, S. Hüttner, T. Leijtens, S. D. Stranks, H. J. Snaith, M. Atatüre, R. T. Phillips and R. H. Friend, *J. Phys. Chem. Lett.*, 2014, **5**, 1421–1426.
- 4 J. Gong, S. B. Darling and F. You, *Energy Environ. Sci.*, 2015, **8**, 1953–1968.
- 5 H. Zhou, Q. Chen, G. Li, S. Luo, T.-b. Song, H.-S. Duan, Z. Hong, J. You, Y. Liu and Y. Yang, *Science*, 2014, **345**, 542–546.
- 6 M. Grätzel, *Nat Mater*, 2014, **13**, 838–842.
- 7 A. Marchioro, J. Teuscher, D. Friedrich, M. Kunst, R. van de Krol, T. Moehl, M. Grätzel and J. E. Moser, *Nat. Photon.*, 2014, **8**, 250–255.
- 8 S. De Wolf, J. Holovsky, S.-J. Moon, P. Löper, B. Niesen, M. Ledinsky, F.-J. Haug, J.-H. Yum and C. Ballif, *J. Phys. Chem. Lett.*, 2014, **5**, 1035–1039.
- 9 C. S. Ponseca Jr., T. J. Savenije, M. Abdellah, K. Zheng,

- A. Yartsev, T. Pascher, T. Harlang, P. Chabera, T. Pullerits, A. Stepanov, J.-P. Wolf and V. Sundström, *J. Am. Chem. Soc.*, 2014, **136**, 5189–5192.
- 10 C. Wehrenfennig, M. Liu, H. J. Snaith, M. B. Johnston and L. M. Herz, *Energy Environ. Sci.*, 2014, **7**, 2269–2275.
- 11 C. Wehrenfennig, G. E. Eperon, M. B. Johnston, H. J. Snaith and L. M. Herz, *Adv. Mater.*, 2014, **26**, 1584–1589.
- 12 L. L. Wang, C. McCleese, A. Kovalsky, Y. X. Zhao and C. Burda, *J. Am. Chem. Soc.*, 2014, **136**, 12205–12208.
- 13 M. Saba, M. Cadelano, D. Marongiu, F. Chen, V. Sarritzu, N. Sestu, C. Figus, M. Aresti, R. Piras, A. Geddo Lehmann, C. Cannas, A. Musinu, F. Quochi, A. Mura and G. Bongiovanni, *Nat. Commun.*, 2014, **5**, 1.
- 14 J. S. Manser and P. V. Kamat, *Nat. Photon.*, 2014, **8**, 737–743.
- 15 V. D’Innocenzo, G. Grancini, M. J. P. Alcocer, A. R. S. Kandada, S. D. Stranks, M. M. Lee, G. Lanzani, H. J. Snaith and A. Petrozza, *Nat. Comm.*, 2014, **5**, 1.
- 16 Q. Lin, A. Armin, R. C. R. Nagiri, P. L. Burn and P. Meredith, *Nat. Photon.*, 2015, **9**, 106–112.
- 17 P. Piatkowski, B. Cohen, F. J. Ramos, M. Di Nunzio, M. K. Nazeeruddin, M. Gratzel, S. Ahmad and A. Douhal, *Phys. Chem. Chem. Phys.*, 2015, **17**, 14674–14684.
- 18 J. A. Christians, P. A. Miranda Herrera and P. V. Kamat, *J. Am. Chem. Soc.*, 2015, **137**, 1530–1538.
- 19 C. Sheng, C. Zhang, Y. Zhai, K. Mielczarek, W. Wang, W. Ma, A. Zakhidov and Z. V. Vardeny, *Phys. Rev. Lett.*, 2015, **114**, 116601.
- 20 C. Zhang, D. Sun, C. X. Sheng, Y. X. Zhai, K. Mielczarek, A. Zakhidov and Z. V. Vardeny, *Nature Physics*, 2015, **11**, 428–435.
- 21 D. W. deQuilettes, S. M. Vorpahl, S. D. Stranks, H. Nagaoka, G. E. Eperon, M. E. Ziffer, H. J. Snaith and D. S. Ginger, *Science*, 2015, **348**, 683–686.
- 22 A. Miyata, A. Mitioglu, P. Plochocka, O. Portugall, J. T.-W. Wang, S. D. Stranks, H. J. Snaith and R. J. Nicholas, *Nat. Phys.*, 2015, **11**, 582–587.
- 23 Z. Guo, J. S. Manser, Y. Wan, P. V. Kamat and L. B. Huang, *Nat. Comm.*, 2015, **6**:7471 doi: 10.1038/ncomms8471.
- 24 C. La-o-vorakiat, T. Salim, J. Kadro, M.-T. Khuc, R. Haselberger, L. Cheng, H. Xia, G. G. Gurzadyan, H. Su, Y. M. Lam, R. A. Marcus, M.-E. Michel-Beyerle and E. E. M. Chia, *Nat. Commun.*, 2015, **6**:7903 doi: 10.1038/ncomms8903.
- 25 T. J. Savenije, C. S. Ponseca, L. Kunneman, M. Abdellah, K. Zheng, Y. Tian, Q. Zhu, S. E. Canton, I. G. Scherblykin, T. Pullerits, A. Yartsev and V. Sundström, *J. Phys. Chem. Lett.*, 2014, **5**, 2189–2194.
- 26 A. Poglitsch and D. Weber, *J. Chem. Phys.*, 1987, **87**, 6373–6378.
- 27 D. G. Cooke, F. C. Krebs and P. U. Jepsen, *Phys. Rev. Lett.*, 2012, **108**, 056603.
- 28 C. C. Stoumpos, C. D. Malliakas and M. G. Kanatzidis, *Inorg. Chem.*, 2013, **52**, 9019–9038.
- 29 Q. Dong, Y. Fang, Y. Shao, P. Mulligan, J. Qiu, L. Cao and J. Huang, *Science*, 2015, **347**, 967–970.
- 30 D. Shi, V. Adinolfi, R. Comin, M. Yuan, E. Alarousu, A. Buin, Y. Chen, S. Hoogland, A. Rothenberger, K. Katsiev, Y. Losovyj, X. Zhang, P. A. Dowben, O. F. Mohammed, E. H. Sargent and O. M. Bakr, *Science*, 2015, **347**, 519–522.
- 31 W. Nie, H. Tsai, R. Asadpour, J.-C. Blancon, A. J. Neukirch, G. Gupta, J. J. Crochet, M. Chhowalla, S. Tretiak, M. A. Alam, H.-L. Wang and A. D. Mohite, *Science*, 2015, **347**, 522–525.
- 32 J. Huang, Y. Shao and Q. Dong, *J. Phys. Chem. Lett.*, 2015, 3218–3227.
- 33 R. A. Kaindl, M. A. Carnahan, D. Hagele, R. Lovenich and D. S. Chemla, *Nature*, 2003, **423**, 734–738.
- 34 M. A. Green, A. Ho-Baillie and H. J. Snaith, *Nat. Photon.*, 2014, **8**, 506–514.
- 35 J. Even, L. Pedesseau and C. Katan, *J. Phys. Chem. C*, 2014, **118**, 11566–11572.
- 36 C. Quarti, G. Grancini, E. Mosconi, P. Bruno, J. M. Ball, M. M. Lee, H. J. Snaith, A. Petrozza and F. D. Angelis, *J. Phys. Chem. Lett.*, 2013, **5**, 279–284.
- 37 F. Brivio, J. M. Frost, J. M. Skelton, A. J. Jackson, O. J. Weber, M. T. Weller, A. R. Goni, A. M. A. Leguy, P. R. F. Barnes and A. Walsh, *arXiv:1504.07508 [cond-mat.mtrl-sci]*, 2015.
- 38 N. Onoda-Yamamuro, T. Matsuo and H. Suga, *J. Phys. Chem. Solids*, 1990, **51**, 1383–1395.
- 39 K. Iwaszczuk, D. G. Cooke, M. Fujiwara, H. Hashimoto and P. U. Jepsen, *Optics Express*, 2009, **17**, 21969–21976.
- 40 P. Umari, E. Mosconi and F. De Angelis, *Sci. Rep.*, 2014, **4**, 1.
- 41 P. Löper, M. Stuckelberger, B. Niesen, J. Werner, M. Filipič, S.-J. Moon, J.-H. Yum, M. Topič, S. De Wolf and C. Ballif, *J. Phys. Chem. Lett.*, 2014, **6**, 66–71.
- 42 X. Wu, M. T. Trinh, D. Niesner, H. Zhu, Z. Norman, J. S. Owen, O. Yaffe, B. J. Kudisch and X. Y. Zhu, *J. Am. Chem. Soc.*, 2015, **137**, 2089–2096.
- 43 T. Suzuki and R. Shimano, *Phys. Rev. Lett.*, 2012, **109**, 046402.



# Intrinsic femtosecond charge generation dynamics in single crystal $\text{CH}_3\text{NH}_3\text{PbI}_3$

## Broader Context

The solar cell community is now fervently exploring the limitations of organohalide lead perovskites for next generation photovoltaics. Fundamental studies of the photophysics of this material are lagging behind the rapid device development, however, and much still needs to be done to understand the basic material properties governing device performance. In this work, we turn the powerful technique of transient multi-THz spectroscopy to study the intrinsic mobile charge generation dynamics in a large single crystal of the prototypical methylammonium lead perovskite or  $\text{MAPbI}_3$ . We use ultra-broadband THz pulses covering a 1 - 135 meV energy range to measure the complex dielectric function, important for its role in estimating the exciton binding energy. Photoexciting at the band-edge, our measurements directly reveal exciton dissociation and mobile charge generation dynamics, efficiencies and mobilities over picosecond time scales with 40 fs resolution. While efficiencies and quasi-equilibrium analysis suggest an exciton binding energy of 50 meV, multi-THz spectra reveal a short-lived intra-excitonic transition indicating a binding energy on the order of 17 meV in the room temperature tetragonal phase. Mobilities as high as  $800 \text{ cm}^2/\text{Vs}$  are measured directly via the frequency-dependent Drude spectra, indicating the polycrystalline morphology of films is a major scattering channel.